The development of internal pressure standards for in-house elastic wave velocity measurements in multi-anvil presses

A. Néri[1,&,*], L. Man[1], J. Chantel[2], R. Farla[3], G. Bauer[1], S. Linhardt[1], T. Boffa Ballaran[1] and D.J. Frost[1]

[1] Bayerisches Geoinstitut, University of Bayreuth, Bayreuth, Germany

[2] Université de Lille, CNRS, INRAE, Centrale Lille, UMR 8207 - UMET - Unité Matériaux et Transformations, F-59000 Lille, France

[3] Deutsches Elektronen-Synchrotron DESY, Hamburg, Germany

[&] Now at Université de Lille, CNRS, INRAE, Centrale Lille, UMR 8207 - UMET - Unité Matériaux et Transformations, F-59000 Lille, France

[*]Corresponding author, e-mail address: adrien.neri@univ-lille.fr

Abstract

Ultrasonic systems are powerful tools to determine wave velocities of minerals and materials at high pressure and temperature, and have been extensively developed in recent decades. However, accurate measurement of sample length is required to convert travel times into wave velocities, limiting their use to synchrotron facilities or room temperature experiments in laboratories. We have made use of a close collaboration between the Bayerisches Geoinstiut and the P61B end-station beamline (PETRA III - DESY) to install ultrasonic systems and develop a novel dual travel time method for *in-situ* pressure determination without the need for synchrotron radiation. Our method relies on the travel times of elastic waves through a reference material; it requires a thermocouple, and is non-intrusive, with the reference material replacing the backing plate of the high-pressure assembly. Pressures obtained from this dual travel time method show excellent agreement with those obtained from X-ray diffraction using synchrotron radiation on standard materials. Our novel method enables *in-situ* pressure determination at varying temperatures during in-house ultrasonic interferometry experiments. This allows not only to determine the elastic behavior of minerals and materials but also to investigate phase diagrams, solidus or liquidus conditions at varying pressure and temperature during in-house experiments.

During the installation of the pulse echo ultrasonic system, we identified critical parameters for obtaining reliable data. While these requirements are well-known to experts, this study presents a comprehensive review of the different characteristics of ultrasonic systems, providing user-friendly guidelines for new users installing and operating such systems in high-pressure and high-temperature conditions.

1. Introduction

Ultrasonic interferometry is a powerful tool for investigating the elastic properties of materials and minerals under pressure and at high temperatures. In recent years, it has been successfully adapted to several pressure generation devices: diamond anvil cells[1], Griggs apparatus[2], piston-cylinder presses[3], Paris-Edinburgh cells[4] and multi-anvil presses[5]. In a typical multi-anvil setup, a piezoelectric crystal is attached to the back of one of the anvils used to apply pressure to the octahedral assembly. A cylindrical sample sits at the center of the assembly between a buffer rod and a backing plate. The piezoelectric crystal sends a compressional (P-) and/or shear (S-) wave pulse through the anvil which then reaches the sample by passing through the hard buffer rod. Due to the acoustic impedance ($Z = \rho v_P$, where ρ is the density and v_P the elastic wave velocity) contrast between the various materials, elastic waves are reflected at interfaces, producing echoes that return to the piezoelectric crystal. The time difference between two successive echoes, from the buffer-rod/sample and the sample/backing plate interfaces, provides the two-way travel time of P- and/or S-waves through the material of interest. An accurate determination of the sample length, pressure, and temperature is critical to properly analyse and extrapolate the collected data. Although temperature can be easily measured by inserting a thermocouple close to the sample, estimating the sample length and pressure is not so straightforward. The sample length can be calculated for instance using Cook's law[6], but this requires precise knowledge of pressure and assumes purely elastic behaviour of the sample, i.e. no significant plastic deformation[7]. Hence, ultrasonic interferometry is a technique that is mostly restricted to synchrotron facilities, where X-ray radiography and diffraction are respectively used *in-situ* to determine the sample length and the pressure from the unit cell volume of reference materials.

Efforts to develop internal pressure standards for in-house experiments have focused on using the travel times of P- and S-waves through the alumina buffer rod (BR)[8]. To do so, previous authors have fitted empirical linear expressions for the pressure and temperature dependences of P- and S-wave travel times, measured using *in-situ* methods. Such parametrizations can, however, only be used for identical assemblies, leaving little room for flexibility in the design, and are likely to be extremely sensitive to temperature gradients within the assembly. An alternative method to such parametrizations is to use the travel times of elastic waves through a reference material with a known $\rho - v_P - v_S - T$ equation of state (EoS), to derive an absolute pressure scale. This method considers the P- to S-wave velocity ratio, to determine the pressure at a given temperature.

For the development of this dual travel time method, pulse-echo ultrasonic systems were installed at the Bayerisches Geoinstitut (BGI) and on the large volume press (LVP) located in the end-station of the high-energy wiggler beamline P61 (called P61B) at the Deutsches Elektronen-Synchrotron (DESY). Although such systems are already used in the high-pressure community[e.g. 9,10], several dimensions and parameters were found to be critical for sweeping through the required frequency range (30-60 MHz), for expanding the accessible temperature range, and for collecting data with very high quality. Hence, this work aims to provide, together with a novel pressure calibration method, clear guidelines for installing ultrasonic interferometry systems and collecting reliable data.

2. Ultrasonic interferometry

2.1 Overview of the systems installed at BGI and on P61B

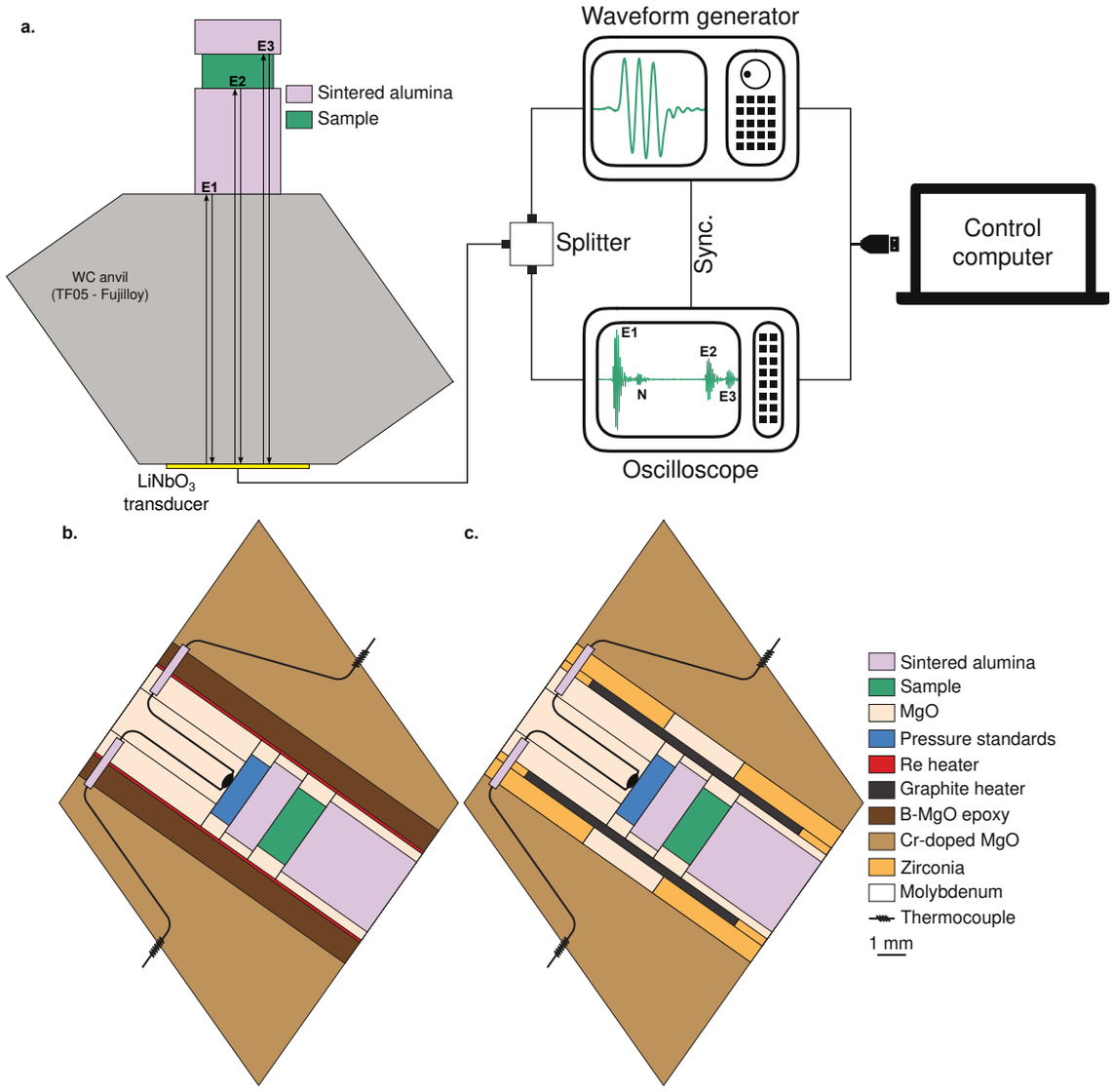

Figure 1 (double-column): (a) Schematic drawing of the ultrasonic systems used both at BGI and at P61B. Due to the acoustic impedance contrast, the elastic waves are reflected along each interface (echoes E1, E2, and E3) and propagate back to the piezoelectric crystal. The oscilloscope records that signal. Both oscilloscope and waveform generator are synchronized together to be on the same time basis (Sync. channel) and are controlled from a computer. (b) and (c) Drawings of the 14/8 (octahedral edge length to cube truncation edge length) multi-anvil assemblies used during the experiment. (b) The rhenium furnace (25 µm foil) allows to use this assembly to pressure up to 15 GPa; the B-MgO epoxy sleeve around the furnace provides good thermal insulation and is X-ray transparent. (c) The graphite heater of this assembly limits the pressure range to 8-10 GPa; here, a MgO ring is sandwiched between two ZrO_2 sleeves to manage an X-ray transparent window.

Ultrasonic wave velocity measurements (e.g. Fig. 1a) are performed following two main methods: (i) the phase comparison method[3,11,12] and the pulse-echo overlap (PEO) method[13,14]. The PEO technique

has been increasingly popular in recent years, mostly due to the simplicity of data analysis and the system required. As such, this study mostly focuses on the pulse-echo overlap method and its application in conjunction with multi-anvil presses.

To generate and measure ultrasonic wave velocities, three main components are required: (i) a $LiNbO_3$ piezoelectric crystal, (ii) an arbitrary waveform generator and (iii) a digital oscilloscope. These components are connected by coaxial cables (Aircell 7) (Fig. 1a). The arbitrary waveform generator (Keysight Trueform 33622A at BGI and Tektronix AFG3152C at P61B) sends bursts of sinusoidal AC pulses (called "sines" in the following) of fixed frequency that are delivered to the oscilloscope and the transducer using a splitter (ZFSC-2-1+, 5-500 MHz, from Mini-Circuits). When subject to this electric signal, the transducer vibrates and generates compressional and/or shear waves, depending on its orientation. For our purpose, oriented 10° Y-cut $LiNbO_3$ crystals (63 µm thick) are used to simultaneously generate P- and S-waves, with resonance frequencies of ≈ 50 and ≈ 30 MHz. In other instances, as in studies of compressional wave velocities of melts, 36° Y-cut crystals can also be used[15,16].

Multi-anvil octahedral assemblies are modified to accommodate a dense sintered alumina "buffer rod" (BR), between the anvil and the sample, and an alumina plate, referred to as the "backing plate" (BP), at the back of the sample (Fig. 1b). As they travel through the assembly, the elastic waves are reflected at the boundaries between different materials due to the acoustic impedance contrasts (echoes E1, E2 and E3, Fig. 1a) and are propagated back to the transducer. The piezoelectric crystal operates as both an emitter and a receiver of ultrasonic waves. Hence, when subject to the reflected waves, it emits electric signals (one for each received echo E1, E2, and E3), that are captured using an oscilloscope (Keysight DSOS054A at BGI and Tektronix MSO64 at P61B). From the collected data, the two-way travel time through the sample is determined from the time difference between the two successive echoes E2 and E3 (Fig. 1a). The waveform generator and oscilloscope are directly connected through a synchronization channel. This additional connection greatly stabilizes the time basis of the oscilloscope by detecting automatically the arrival of the initial pulse; this feature is essential when averaging signal time frames, as changes in the time basis during spectra collection induce a strong bias in the signal.

Low porosity dense sintered alumina is used for both the BR and BP to limit the scattering of the waves and to preserve the flatness of the sample-BR and sample-BP interfaces. These parts thus ensure that the interfaces remain perpendicular to the wave propagation front direction and that elastic waves back-propagate in the right direction. Furthermore, alumina was chosen due to its high acoustic impedance contrast with our sample materials, enhancing the amplitude and the sharpness of wave reflections along these interfaces.

Data collection has been automated, via an in-house LabView-based GUI at BGI, and by adapting existing Python-based scripts[9] at P61B. During this automated procedure, it is crucial to sweep through the frequency range to identify potential travel time dependence on the frequency (see Supplementary Material S.1 and Fig. S.1). As such, the frequency range to sweep, the number of sines to be sent in the burst and the number of time frame averages to be collected can be tuned before starting data collection. From the collected data, the two-way travel time through the sample, or any part of interest, is determined from the time difference between two successive echoes. To calculate this time difference,

a LabView-based GUI was produced by G. Bauer, based on a correlation function. A reference echo is selected, for instance, the echo between the cube and the BR (E1), and is correlated through a time region of interest (taken as the P- or S-wave time regions). The resulting correlation function shows a series of maxima and minima, where the time difference between the extrema of successive echoes yields the two-way travel times of interest. However, when doing so, care should be taken to identify potential phase inversions, which occur when there is a change in the sign of the acoustic impedance contrast between two successive interfaces (from material 1 to material 2: $\Delta Z = \frac{\rho_2 v_{P_2} - \rho_1 v_{P_1}}{\rho_2 v_{P_2} + \rho_1 v_{P_1}}$, with ρ and v_P the density and P-wave velocity of material 1 and 2). These phase inversions can usually be identified by visual inspection of the successive echoes. In case of a phase inversion, maxima should be correlated with minima or vice-versa.

2.2 Technical development – A matter of sizes

Two important parameters need to be considered when conducting ultrasonic interferometry experiments: (i) the size of the tungsten carbide (WC) anvils and (ii) the transducer diameter. Both dimensions are discussed in the following and are found to be hard to reconcile together. Compromises to optimize the strength and quality of the signal are proposed based on the size of the assembly.

The size of the anvil should be small enough to preserve the high-frequency signal (40-60 MHz), but not too small since the anvil length controls the time separation between P- and S-wave trains and avoids, therefore, the overlap of different echoes. Although acoustic waves are in principle “elastic”, in the sense that they elastically deform the medium through which they propagate, they still get dispersed and lose energy. High-frequency waves, i.e. shorter wavelengths, require more cycles to travel through a fixed distance than low-frequency ones. At high frequencies, elastic waves thus lose more energy and tend to vanish rapidly. For 54 mm edge length (EL) anvils, only the low-frequency range is accessible (10-20 MHz), for 32 mm EL anvils, the frequency is slightly extended to ≈ 40 MHz, the whole frequency range (up to 60 MHz) is only accessible for anvils of 26 mm EL or less, which is the standard anvil size used for multi-anvil experiments at synchrotron facilities.

From the piezoelectric source, the wave propagation profile is generally divided into two zones: the near field and the far field. The near field, also corresponding to the Fresnel zone, is the closest region to the source, i.e. the piezoelectric crystal, where the acoustic pressure profile goes through a series of maxima and minima (see Fig. S.2a). The location of the last minimum, i.e. of the last destructive interference, defines the length of the near field. Beyond that lies the far field, in which the acoustic pressure profile gradually increases to a last maximum before decreasing to zero through attenuation processes (diffraction, scattering, and absorption). The length of the near field N depends on the diameter of the transducer ϕ_{LiNbO_3}, the signal frequency f and the anvil velocity v_P (taken to be ≈ 6800 m.s^{-1} through the anvil used in this study) according to the relation $N = \frac{\phi^2_{LiNbO_3} f}{4 v_P}$ (see Supplementary Material S.2 for the derivation of this equation). The curves plotted in Fig. 2a represent the transition from the near field to the far field as a function of the transducer diameter and for different frequencies. Because the acoustic pressure fluctuates in the near field, the anvil-BR, BR-sample, and sample-BP reflections should be located well within the far field, i.e. the path length of the waves producing the

anvil-BR echo should lie above the curves drawn in Fig. 2a. For example, considering 26 mm EL anvils equipped with 8 mm truncations, this condition would only be reached for small transducers, below ≈ 4 mm (Fig. 2a). The transducer diameter also determines its resistance, which should not deviate too much from the resistance of the whole ultrasonic system (most waveform generators and oscilloscopes have a fixed resistance of 50 ohms) to minimize the impedance mismatch between transducer and hardware. By trial and error, the ideal transducer diameter for an optimal resistance match and signal quality between 30 and 60 MHz was found to be ≈ 2.5 mm.

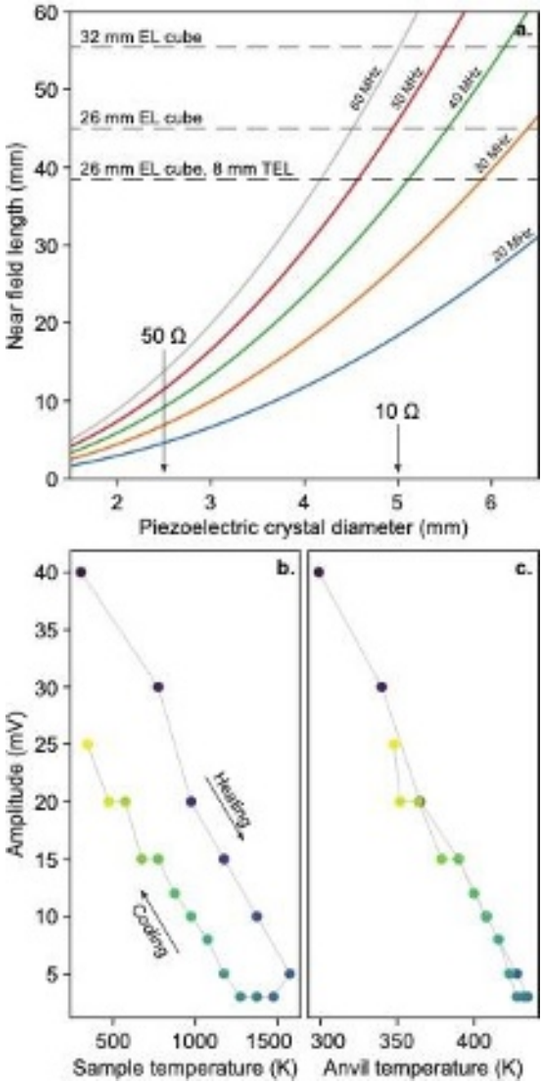

Figure 2 (single column): (a) Length of the Fresnel zone ($N = \frac{\phi_{LiNbO_3} f}{4 v_P}$, with ϕ_{LiNbO_3}, f and v_P the diameter of the transducer, the pulse frequency and the elastic wave velocity through the anvil, respectively) as a function of the transducer diameter at different fixed frequencies (see Supplementary Material S.2). The length of the Fresnel zone denotes the distance to the last acoustic pressure minimum. Vertical arrows show the resistance of transducers with 2.5 and 5 mm diameter. The anvil-BR echo should ideally be located outside of the Fresnel zone, which is matched with an ideal resistance for transducer diameters of 2.5 mm. (b) and (c) amplitude of the BR-sample reflection as a function of the sample and anvil temperature, respectively. The temperature of the transducer should be controlled to a certain extent, to limit the amplitude drop and expand the temperature of collectable data.

Small transducers, of ≈ 2.5-4.0 mm in diameter, thus seem to be the best choice, having a good impedance match and placing the location of the reflections of interest within the far field. Larger transducers, which can be preferred for large cube truncations and because they are easier to handle, may still be used. However, the accessible frequency range may be limited during the time of the experiment, as described below and in Supplementary Material S.1 (Fig. S.1).

2.3 Anvil temperature and transducer efficiency

The performance of the piezoelectric crystal degrades with increasing temperature. The precise effect of temperature on the piezoelectric properties of lithium niobate is difficult to assess as it drastically depends on the precise composition of the crystal. Depending on manufacturers, the lithium-to-niobium ratio can slightly deviate from unity, and magnesium can be used as a stabilizer. However, two main effects can be qualitatively addressed to discuss the evolution of the piezoelectric properties of lithium niobate as a function of temperature. The first is apparent in studies using optical methods to examine single crystals of $LiNbO_3$ as a function of temperature. Drastic changes in optical features indicate two phase transitions, a first at 343-363 K and a second at 383-393 K[17]. The phase transitions likely affect the resistance and piezoelectric properties, but are entirely reversible upon cooling. The second effect that causes a decrease in the piezoelectric properties with temperature is the increase in the electrical conductivity of the crystal[18]. To generate the elastic waves, a voltage difference is imposed between the two opposite faces of the $LiNbO_3$ crystal. Since the electrical conductivity of the transducer increases with temperature, the charge carriers are mobilized and leak across the crystal to re-equilibrate the voltage potential between opposite faces, giving rise to a smaller voltage difference than that imposed from the initial signal. As a consequence, the crystal vibrates with less energy and the amplitude of elastic waves thus decreases. This charge leakage effect depends on the crystal dimensions (width and thickness) and the frequency of the input signal and can be reduced by using lower frequencies and thicker crystals.

To monitor these effects, the temperatures in the sample region and that on the anvil that bears the transducer were recorded during an experiment (Fig. 2b,c). The amplitude of the ultrasonic signal indeed decreases smoothly upon heating but increases on cooling. This amplitude drop is entirely reversible when compared to the anvil temperature but is delayed when compared to that of the sample, most likely due to the sluggish heat diffusion between the assembly and the piezoelectric crystal. From the smooth decrease in amplitude as a function of the anvil temperature, it seems that the charge leakage through the crystal is the primary effect responsible for the observed amplitude drop.

Since the crystals used for ultrasonic interferometry coupled with a multi-anvil apparatus need to be thin (63 µm) for generating high-frequency (MHz) waves on anvils that heat up to over 420 K when the sample is heated to high temperatures, a possible way for limiting the deterioration of the ultrasonic signal during the time of the experiment and to expand the accessible temperature range is to use a vortex cooling gun (Coldstream Air Gun from Meech) to blow focused cooled air (≈ 280 K) onto the surface of the transducer. A cooling gun has been mounted on an articulated arm to accommodate the geometry of the Aster-15 6-ram Hall-type LVP at P61B. The articulated arm is directly attached to one of the rams, and can thus move along with the ram so that the cooled air is always focused between three of the first-stage anvils. This vortex cooling gun expands the range of data collection, up to sample

temperatures of ≈ 2100 K for 14/8 assemblies (OEL to cube truncation edge length). The use of cooling guns is also likely to extend the accessible temperature range even more for smaller assemblies.

3. Elastic wave velocities of San Carlos-like olivine

To examine the efficiency and the quality of data obtained from the ultrasonic interferometry system installed at P61B, the elastic properties of a mantle olivine composition (90% of forsterite composition, noted Fo_{90}, see Supplementary Material S.3 for sample synthesis) were investigated. Experiments were conducted on the Aster-15 large volume press installed on P61B, in combination with synchrotron radiation (the detector setup and beamline capabilities are described elsewhere)[19]. The 14/8 assembly equipped with a rhenium heater was used to collect data in the 8-13 GPa range and up to 1500 K (experiment BT530), while the 14/8 assembly equipped with a graphite furnace was used to collect data up to 8 GPa and up to 1650 K (experiment BT613). To test the feasibility of using transducers with large diameters, 6.35 mm (BT530) and 5 mm (BT613, similar to [20]) piezoelectric crystals were used in combination with these 14/8 assemblies.

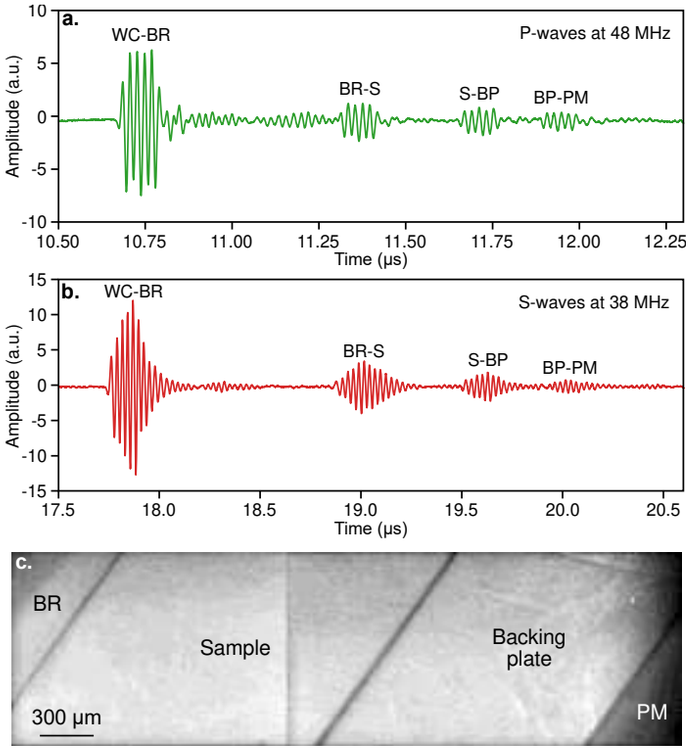

Figure 3 (double column): (a) and (b) Typical P- and S-wave ultrasonic echo trains. These signals correspond to data collected during BT613 at conditions of 120 bar of oil pressure load and 1173 K. These signals are represented at frequencies of 48 MHz for the P-waves and 38 MHz for the S-waves and correspond to the frequencies at which travel times were measured (see Supplementary Material S.1). (c) Typical radiography image collected during BT613 at the same conditions as (a) and (b). This image corresponds to two images stitched together, one that is centered on the sample and one that is centered on the backing plate. BR denotes the buffer rod and PM the XRD pressure markers.

Bursts composed of 3 sines at varying frequencies (14-50 MHz) were sent to the piezoelectric crystal to generate P- and S-waves. Examples of raw signals for P- and S-waves and X-ray radiography are

reported in Fig. 3. From the time-amplitude spectra captured by the oscilloscope (Fig. 3a,b), the two-way travel time through the olivine sample was calculated using the PEO method. The sample length is measured using X-ray radiography (Fig. 3c). On each radiographic image, the average grayscale profile perpendicular to the sample direction is computed, and the sample length is determined from the distance between the two absorption maxima caused by the thin Pt foils (2 µm) on both ends of the sample. The acoustic wave velocities for both P- and S-waves can then be calculated and plotted as a function of the density obtained from the X-ray diffraction data (see Supplementary Material S.4 for the description of XRD data analysis, Fig. 4a,b and Table S.2). Uncertainties on the sample length (taken to be within 5 pixels of the absorption maxima; pixel size of 1.44 µm) and on the two-way travel time (corresponding to two standard deviations over the frequency range) are propagated to obtain the uncertainties in wave velocities, whereas the uncertainty on the density is estimated from the fit uncertainty of the unit cell volume as provided by GSAS-II[21]. At constant load, the wave velocities and density of olivine decrease linearly with increasing temperature, in agreement with the expected behaviour of olivine at high pressure and high temperature (Fig. 4a,b).

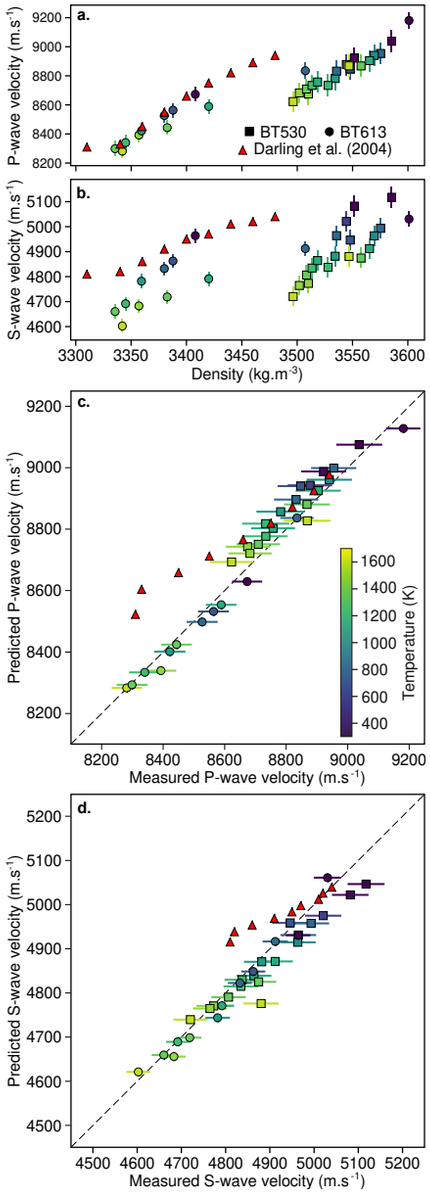

Figure 4 (single column): (a) P- and (b) S-wave velocities of Fo_{90} olivine as a function of density and temperature (color code). Elastic wave velocities increase with density and decrease with temperature. (c) and (d) Comparison between the measured elastic wave velocities and the values that would be predicted from our EoS fit. Ideally, all data should align on a 1:1 line, which seems to be the case for S-waves (d) but not for the P-waves measured on BT530 (c). This is likely due to the limited frequency range that could be swept on the transducer used during the BT530 experiment, causing an apparent larger travel time, and thus a lower measured velocity. Horizontal bars correspond to two standard deviations. Red triangles show data collected using Cook's law at room temperature[30].

To compare our velocity data with the existing EoS of Fo_{90} olivine, a fit of literature data[22–26] was conducted using a Birch-Murnaghan EoS with a Mie-Grüneisen-Debye thermal model[27,28] (see Supplementary Material S.5 and S.7 for details). When comparing the collected elastic wave velocities to that predicted from the fit parameters (Fig. 4c,d), the data acquired for the BT613 experiment align almost perfectly along a 1:1 line for both P- and S-waves, while only the S-wave velocities seem to follow this 1:1 line for BT530. The reason for this apparent shift in the P-wave velocities is due to the limited frequency range used to collect data during the BT530 experiment (up to 40 MHz, see Supplementary Material S.1 and Fig. S.1). Indeed, due to the large size of the piezoelectric crystal used, 6.35 mm, the maximum frequency for P-wave travel time measurement is limited to 40 MHz (see Fig. 2a), while larger frequencies of ≈ 50 MHz are necessary to reach the steady state where travel time is no longer frequency dependent. This effect is only visible for the P-waves as the steady state for S-waves is reached at a lower frequency ≈ 30 MHz. The use of smaller transducers can solve this issue, as seen with the data collected during BT613, where a 5 mm crystal was used. The data collected during the BT530 experiment are shown here to draw attention to the need for small and high-quality piezoelectric crystals to precisely measure P- and S-wave velocities.

Although the velocity data represented in Fig. 4 are not corrected for the platinum bond that is inserted between the sample and the BR or BP, they are in excellent agreement with what can be predicted from other techniques. It has recently been proposed that the bond correction has a vanishingly small impact on travel times for extremely small bond thicknesses and large sample lengths[29]. Our experiments are well inscribed within these criteria, with 2 µm thin bonds and samples larger than 1 mm.

Red triangles (Fig. 4) show existing literature data[30] that were collected at room temperature using Cook's method[6] in a multi-anvil apparatus. When comparing these velocity data with what would be expected from our EoS parameters (Fig. 4c,d), only the high load data points seem to fall onto the 1:1 line. In their study, the authors argue that the data collected at low load data might be biased due to an incomplete mechanical coupling between the sample and the surrounding parts. When Cook's law[6] is used, the sample length is estimated from the measured P- and S-wave travel times. Hence, at low load, the presence of residual pores due to incomplete sintering may also affect the P- and S-wave travel times and the predicted sample lengths, shifting the elastic wave velocities compared to our EoS parameters. When the load is high enough and the residual porosity is entirely closed, elastic wave velocities perfectly align along the 1:1 line.

4. Internal pressure standards for in-house ultrasonic measurements

4.1 The dual travel time method to determine pressure *in-situ*

P- and S-wave velocities, v_P and v_S, can be expressed as follows:

$$v_P = \frac{l}{t_P} = \sqrt{\frac{K_S(P,T)+\frac{4}{3}G(P,T)}{\rho}}, \quad (1)$$

$$v_S = \frac{l}{t_S} = \sqrt{\frac{G(P,T)}{\rho}}, \quad (2)$$

with l and ρ being the length and density of the reference material, t_P and t_S the P- and S-wave travel times, K_S and G the adiabatic bulk and shear moduli, which are functions of pressure P and temperature T. While temperature can be monitored by a thermocouple during the experiments, the length and density of the reference material cannot be directly determined during in-house experiments. Dividing equation (1) by equation (2) removes the dependence on the length and density of the reference material, and is equivalent to the S- to P-wave travel time ratio:

$$\frac{v_P}{v_S} = \frac{t_S}{t_P} = \sqrt{\frac{K_S(P,T)}{G(P,T)}+\frac{4}{3}}. \quad (3)$$

Hence, at a given temperature, variations in the P- to S-wave velocity ratio, i.e. in the S- to P-wave travel time ratio, are controlled by pressure. By simultaneously monitoring temperature, and the dual travel time of P- and S-waves through a reference material of known $\rho - v_P - v_S - T$ EoS, equation (3) can be solved to determine the pressure inside the assembly at a given temperature. A precise measurement of the initial unit cell volume is critical to obtain precise pressure values, which can be done through X-ray diffraction of the starting powder under ambient conditions.

This dual travel time method constitutes a non-intrusive technique to determine pressure *in-situ* without requiring synchrotron radiation. The simplicity of equation (3) makes it computationally very efficient to solve and easy to use. To reduce the uncertainty of the pressure estimation, the P- to S-wave velocity ratio, i.e. the adiabatic bulk to shear modulus ratio, should have a large dependence on pressure at a given temperature. Fig. 5a shows the evolution of the P- to S-wave velocity ratio as a function of pressure for several minerals or materials of known $\rho - v_P - v_S - T$ EoS (Fo_{90} olivine, MgO, and Al_2O_3) along two different isotherms (300 K as full-line and 1300 K as dashed line). As detailed below, Fo_{90} olivine shows the largest sensitivity of its S- to P-wave travel time ratio as a function of pressure. Thus, it is found to be the most promising candidate at pressures up to 14 GPa for both room and high temperatures. The pressure dependence of the P- to S-wave velocity ratio is smaller for MgO and Al_2O_3 (Fig. 5a). These materials can still be used for our dual travel time method, but larger uncertainties are to be expected on the pressure values obtained (see Section 4.3). Interestingly, the P- to S-wave velocity ratio is more sensitive to pressure at high temperatures (Fig. 5a), thus this method is expected to be more precise when high-temperature data are to be collected (see Section 4.3).

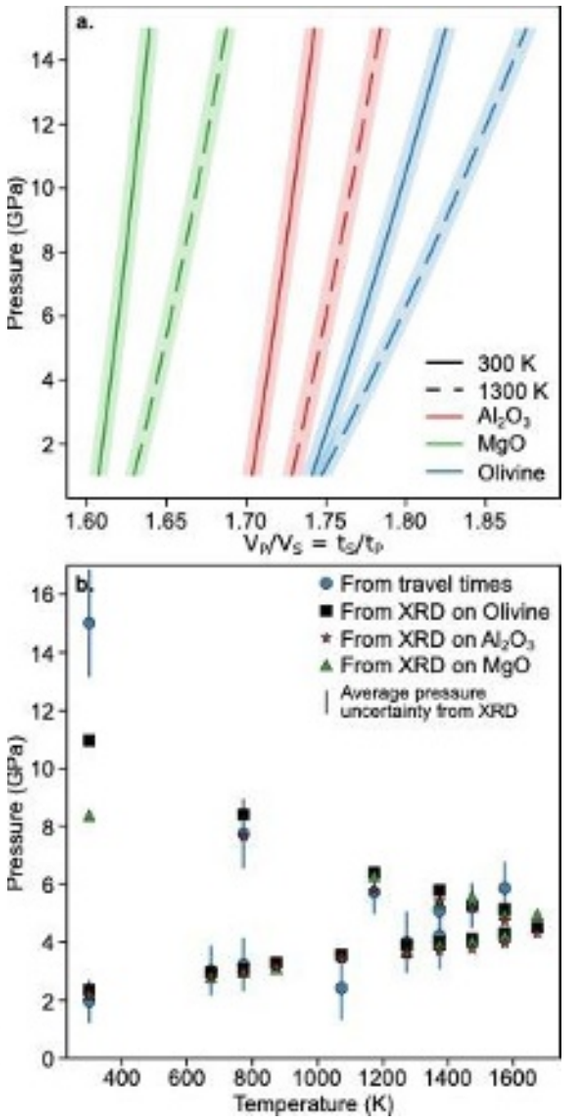

Figure 5 (single column): (a) Pressure evolution of the P- to S-wave velocity ratio (equivalent to the S- to P- wave travel time ratio) for Fo_{90} olivine, MgO, and Al_2O_3, and along two isotherms (300 K in full line and 1300 K in dashed line). This synthetic case was conducted using our EoS fit parameters for Fo_{90} olivine, and existing EoS literature data for MgO and Al_2O_3[28]. Shaded areas correspond to the uncertainty envelopes caused by the propagation of typical uncertainties on the P- and S-wave travel times (see Supplementary Material S.8). (b) Comparison of the pressures determined from *in-situ* X-ray diffraction data of standard materials and our novel dual travel time method, as a function of temperature. Due to small signal amplitudes at the highest temperatures and during the first steps of cooling, travel times could not be properly estimated and these data points are thus not represented. Vertical lines denote two standard deviations in pressure from the uncertainty on the travel time ratios (see Supplementary Material S.8).

4.2 Comparison with classical methods

The feasibility of this dual travel time technique using Fo_{90} olivine has been tested against the data collected during the experiment BT613.

Pressure has been determined using the unit cell volumes measured *in-situ* for MgO with an existing EoS[31], for the α-Al_2O_3 backing plate in combination with our literature fit (see Supplementary Material S.6 and Table S.1 for the fit parameters), and for the Fo_{90} olivine sample itself along with the Reuss bound of our fit parameters (see Supplementary Material S.7 and Table S.3 for the fit parameters). A comparison of the pressures obtained based on these three sensors and from our dual travel time method is shown in Fig. 5b, as a function of temperature. After the initial cold compression and just before heating, none of the pressure sensors agreed. As soon as heating starts, all materials give similar pressures, but the agreement is even better during the cooling path. It seems here that the differential compressibility of materials within the assembly causes a lot of stress, which is released when the experiment is annealed above 800 K. It can be noted that the pressures estimated from the dual travel time method are not shown for the highest temperature points. The cooling on the surface of the transducer was not efficient enough and the data collected at the highest temperatures show very low amplitudes, therefore the correlation function is unable to properly find the extrema. Uncertainties evaluated using random Monte Carlo propagations are reported in Fig. 5b (see Supplementary Material S.8 for details). Typical uncertainties on the pressure estimated obtained using the unit cell volume of reference materials are on the order of ± 0.4 GPa, while those from the dual travel time method are on the order of ± 1 GPa but vary with temperature (see Section 4.3).

Overall, Fig. 5b demonstrates the feasibility and reliability of the dual travel time method for estimating pressure. However, it should be noted that for this technique to work properly, the equation of state of the reference material has to be well constrained and the travel times have to be measured in the appropriate frequency range. If for instance, this exercise was to be conducted on BT530, for which the limited frequency range gives erroneous apparent P-wave travel times (≈ 1.3-1.7% higher than the real value from the sigmoid fit on Fig. S.1), the dual travel time method would yield pressure estimates that are 3 to 4 GPa lower than pressure estimates from the XRD calibrants.

4.3 Uncertainties and limitations

Shaded areas in Fig. 5a denote the uncertainty associated with pressures determined using the dual travel time method (see Supplementary Material S.8 for a description of uncertainty evaluation). Typical uncertainties on travel times correspond to 0.4 % for the P-waves and 0.2 % for the S-waves, yielding an uncertainty of ≈ 0.5 % on the S- to P-wave travel time ratio (± 0.008 in absolute values). The impact of that travel time ratio uncertainty on the estimation of pressure depends on the material, and more precisely on the sensitivity of the travel time ratio to pressure (Fig. 5a). An additional degree of difficulty is that the sensitivity of the travel time ratio depends on temperature. In the worst-case scenario, corresponding to MgO and Al_2O_3 at room temperature, where the travel time ratio is not very sensitive to pressure, a travel time ratio uncertainty of ± 0.5 % corresponds to a pressure uncertainty of ± 3 GPa. At higher temperatures (1300 K), the travel time ratio is more pressure-sensitive, halving the pressure uncertainty to ± 1.5 GPa. For Fo_{90} olivine, the room temperature pressure-sensitivity of the dual travel time method is similar to the high-temperature one of MgO and Al_2O_3, yielding pressure uncertainties on the order of ± 1.3 GPa. Here also, the travel time ratio is increasingly sensitive to pressure with temperature, and the pressure uncertainty becomes ± 0.7 GPa at 1300 K. The temperature-sensitive uncertainties for olivine are reported in Fig. 5b.

Based on these predictions and to emphasize the description made in Section 4.1, the material to be chosen as an internal pressure standard is crucial. The S- to P-wave travel time ratio should be as sensitive as possible to pressure to yield the best accuracy and precision possible. As such, MgO and Al_2O_3 seem to be poor choices due to the low sensitivity of the travel time ratio to pressure, hence the large uncertainties associated with the pressure estimates. Although olivine can be used over a narrower pressure range (up to 14 GPa), due to phase transitions, it shows the largest sensitivity of the travel time ratio to pressure and thus constitutes the most promising candidate investigated here.

Due to the sensitivity of the pressure estimates on the measured travel times, two main precautions have to be considered to obtain reliable pressure estimates. Firstly, the pressure standard material has to be under hydrostatic conditions. As such, it is recommended to anneal the assembly after any compression step, to release deviatoric stresses. Any deviatoric stress is likely to cause S- to P-wave travel time ratios that deviate from what is predicted from the EoS, thus yielding unreliable pressure estimates. Secondly, the disk of reference pressure material has to be composed of randomly oriented grains, so that it constitutes a macroscopically isotropic material with not preferred orientations. If the material shows a preferred orientation, then the travel time ratio is also likely to deviate from what can be predicted from the EoS and give an erroneous pressure estimation. Thus, sintering of the disk of reference material should be conducted with limited deformation to avoid the formation of oriented structures. Moreover, grain growth can also result in the acquisition of preferred orientations, and should thus be as limited as possible. It is of note that the large grain-scale anisotropy[32] and fast growth kinetics[33] of MgO make it likely to obtain a preferred orientation during an experiment. Hence, MgO seems to be a problematic material to use as an internal pressure standard.

With these limitations in mind and by taking the appropriate precautions, not only are we able to prove that the measured travel times are consistent with data collected using different techniques (Fig. 4c,d) but also the dual travel time method gives pressure estimates that are in excellent agreement with conventional techniques (Fig. 5b).

4.4 The use of the dual travel time method with another sample

The dual travel time method constitutes a powerful tool that provides a non-intrusive way to estimate pressure *in-situ*, without requiring synchrotron radiation. The assessment of the feasibility of this technique has been conducted using olivine at the sample position to be able to measure accurately its length during compression. However, when used as an internal standard in an in-house experiment, olivine would be used as the backing plate. This is possible, since, as shown in Fig. 3, the reflections on both ends of the BP are well separated and since the amplitude of the reflection at the back of the BP is still large enough to accurately determine its travel time.

In this study, the proof of concept has been conducted on Fo_{90} olivine, but other materials can also be used to extend the accessible pressure range, provided these materials have an S- to P-wave travel time ratio that is sensitive to pressure. Note that the location of the reference material, of well-known EoS, relative to the sample is highly versatile: it can either be placed at the back of the sample and constitute the backing plate or at the front of the sample. While placing the reference material as the backing plate is best suited for most applications, some applications may require placing the reference material between the buffer rod and the sample, as, for instance, in the case of partially molten systems

(see below). Pressure can thus be determined from the ratio of the P- and S-wave travel times through the reference material, and the travel times through the sample can be simultaneously used to determine elastic wave velocities or to investigate phase transitions.

To conduct in-house elastic wave velocity measurements, it is crucial to know the sample length. Without synchrotron radiation, Cook's law[34] is often used. The limitation of this method depends on an accurate pressure determination, often requiring tedious pressure calibrations to be carried out beforehand. Our dual travel time method offers a simplified solution, where pressure is determined *in-situ* in the same experiment, making it possible to use Cook's law[34] even at high temperatures, provided that some information on the thermal expansion and Grüneisen parameter of the material under study is known.

When a phase transition occurs, a volume contraction is often accompanied by a stiffening of the elastic constants, while a volume expansion is accompanied by a softening of the elastic moduli. These effects lead to sudden and drastic changes in the travel time of elastic waves through the sample. As the precise pressures can be determined by our newly established technique, at different loads and temperatures in a single experiment, a P-T phase diagram can be efficiently established in fewer runs.

Similarly, melting drastically affects the P- and S-wave travel times. Thus, the evolution of the solidus and liquidus conditions with pressure can also be investigated during in-house experiments, with our dual travel time method. Solidus conditions can be determined by the sudden drop in the P- and S-wave travel times through the sample, upon increasing temperature[35,36]. In the partially molten state, the presence of small crystals is most likely causing a strong scattering of the P-waves and a decrease in the amplitude of the reflection. Upon complete melting and with the disappearance of these crystals, the amplitude of the P-wave reflection at the back of the sample increases back up and is accompanied by the disappearance of the S-wave reflection, marking liquidus conditions[35]. As mentioned, the presence of interfaces between the liquid and solid grains causes a lot of scattering. Hence, it may prove difficult to properly identify the echoes on the reference material if the signal is already strongly attenuated across the sample. In this particular case, it may be recommended to place the reference material between the sample and the buffer rod, to keep the reflections as strong as possible on both ends of the reference material.

5. Conclusion

In this study, several critical parameters that affect elastic wave velocity measurements in large-volume presses have been examined. The size of the anvils used not only affects the accessible frequency range but is also involved in a subtle interplay with the transducer size that affects the quality of the reflections within the assembly. Overall, the use of small anvils (26 mm EL or less) and small piezoelectric crystals (2.5-4.0 mm in diameter) is highly recommended. It is also critical to cool the transducer externally if high-temperature data are to be collected.

A novel dual travel time method is presented to determine pressure from the travel time of elastic waves through a reference material. This method requires a thermocouple to measure temperature close to the sample, and the initial unit cell volume or density of the reference material. It is not an intrusive technique, as the reference material can simply be placed at the back of the sample and constitute the backing plate. An excellent agreement is found between pressures obtained from this dual

travel time method and more conventional *in-situ* techniques involving synchrotron radiation (X-ray diffraction). The use of our novel method allows *in-situ* pressure determination for in-house ultrasonic interferometry experiments.

In addition, travel times through the sample can also be monitored from the collected data to track travel time sensitive processes as a function of pressure, temperature, or even time. Monitoring the travel time changes can enable the investigation of solid phase transitions or melting phase relations. Hence, it also constitutes a powerful tool to investigate phase diagrams or melting phase relations as a function of pressure and temperature during in-house experiments.

Supplementary Material

Supplementary Material to this article can be found online. These materials provide all the data used in this study along with extensive descriptions of sample synthesis, data analysis, fitting procedures and evaluation of uncertainties.

Acknowledgements

Two anonymous reviewers are thanked for their constructive comments that improved the quality of the manuscript. The authors are very grateful for the invaluable support of the technical staff in BGI: H. Fischer and S. Übelhack for machining assembly parts and steel support to attach transducers, and R. Njul and A. Röther for sample preparation. We also wish to thank S. Sonntag (P61B, DESY) for suggesting and implementing the articulated arm on which the cooling gun is installed, and S. Bhat (P61B, DESY) for insightful discussions on detector positions and suggesting the press rotation. We are thankful to K, Nishida for thoughtful discussions on ultrasonic interferometry setups and measurements. We acknowledge DESY (Hamburg, Germany), a member of the Helmholtz Association HGF, for the provision of experimental facilities. Parts of this research were carried out at beamline P61B (Proposal No. 20210323, and 20211477) with support from the Federal Ministry of Education and Research, Germany (BMBF, grants no.: 05K16WC2 & 05K13WC2). This work was funded through DFG grant FR1555/11.

1. Jacobsen, S. D. *et al.* Gigahertz ultrasonic interferometry at high P and T : new tools for obtaining a thermodynamic equation of state. *Journal of Physics: Condensed Matter* **14**, 11525–11530 (2002).
2. Moarefvand, A. *et al.* A new generation Griggs apparatus with active acoustic monitoring. *Tectonophysics* **816**, 229032 (2021).
3. Niesler, H. & Jackson, I. Pressure derivatives of elastic wave velocities from ultrasonic interferometric measurements on jacketed polycrystals. *J Acoust Soc Am* **86**, 1573–1585 (1989).
4. Kono, Y., Yamada, A., Wang, Y., Yu, T. & Inoue, T. Combined ultrasonic elastic wave velocity and microtomography measurements at high pressures. *Review of Scientific Instruments* **82**, 2–5 (2011).
5. Li, B., Kung, J. & Liebermann, R. C. Modern techniques in measuring elasticity of Earth materials at high pressure and high temperature using ultrasonic interferometry in conjunction with synchrotron X-radiation in multi-anvil apparatus. *Physics of the Earth and Planetary Interiors* **143**, 559–574 (2004).
6. Cook, R. K. Variation of Elastic Constants and Static Strains with Hydrostatic Pressure: A Method for Calculation from Ultrasonic Measurements. *J Acoust Soc Am* **29**, 445–449 (1957).
7. Chantel, J., Mookherjee, M. & Frost, D. J. The elasticity of lawsonite at high pressure and the origin of low velocity layers in subduction zones. *Earth Planet Sci Lett* **349–350**, 116–125 (2012).
8. Wang, X. *et al.* Acoustic travel time gauges for in-situ determination of pressure and temperature in multi-anvil apparatus. *J Appl Phys* **118**, 065901 (2015).
9. Jing, Z., Yu, T., Xu, M., Chantel, J. & Wang, Y. High-Pressure Sound Velocity Measurements of Liquids Using In Situ Ultrasonic Techniques in a Multianvil Apparatus. *Minerals* **10**, 126 (2020).
10. Higo, Y., Irifune, T. & Funakoshi, K. I. Simultaneous high-pressure high-temperature elastic velocity measurement system up to 27 GPa and 1873 K using ultrasonic and synchrotron X-ray techniques. *Review of Scientific Instruments* **89**, (2018).
11. Rigden, S. M., Jackson, I., Niesler, H., Ringwood, A. E. & Liebermann, R. C. Pressure dependence of the elastic wave velocities for Mg2GeO4 spinel to 3 GPa. *Geophys Res Lett* **15**, 605–608 (1988).
12. Rigden, S. M., Gwanmesia, G. D., Jackson, I. & Liebermann, R. C. Progress in High-Pressure Ultrasonic Interferometry, the Pressure Dependence of Elasticity of Mg2SiO4 Polymorphs and Constraints on the Composition of the Transition Zone of the Earth's Mantle. in *High-Pressure Research: Application to Earth and Planetary Sciences* 167–182 (American Geophysical Union (AGU), 1992). doi:https://doi.org/10.1029/GM067p0167.
13. Papadakis, E. P. Ultrasonic Phase Velocity by the Pulse-Echo-Overlap Method Incorporating Diffraction Phase Corrections. *J Acoust Soc Am* **42**, 1045–1051 (1967).
14. Papadakis, E. P. Absolute Accuracy of the Pulse-Echo Overlap Method and the Pulse-Superposition Method for Ultrasonic Velocity. *J Acoust Soc Am* **52**, 843–846 (1972).
15. Nishida, K. *et al.* Effect of sulfur on sound velocity of liquid iron under Martian core conditions. *Nat Commun* **11**, 1–5 (2020).
16. Nishida, K. *et al.* Sound velocity measurements in liquid Fe-S at high pressure: Implications for Earth's and lunar cores. *Earth Planet Sci Lett* **362**, 182–186 (2013).
17. Jiaping, C. & Lamei, W. Study of Phase Transition in Doped LiNbO3 Crystal by Optical Method. *Jpn J Appl Phys* **24**, 248 (1985).
18. Lucas, K., Bouchy, S., Bélanger, P. & Zednik, R. J. High-temperature electrical conductivity in piezoelectric lithium niobate. *J Appl Phys* **131**, (2022).
19. Farla, R. *et al.* Extreme conditions research using the large-volume press at the P61B endstation, PETRA III. *J Synchrotron Radiat* **29**, 409–423 (2022).
20. Nishida, K. *et al.* Effect of sulfur on sound velocity of liquid iron under Martian core conditions. *Nat Commun* **11**, 1–5 (2020).
21. Toby, B. H. & Von Dreele, R. B. GSAS-II : the genesis of a modern open-source all purpose crystallography software package. *J Appl Crystallogr* **46**, 544–549 (2013).
22. Zha, C., Duffy, T. S., Downs, R. T., Mao, H. & Hemley, R. J. Brillouin scattering and X-ray diffraction of San Carlos olivine: direct pressure determination to 32 GPa. *Earth Planet Sci Lett* **159**, 25–33 (1998).
23. Zhang, J. S. & Bass, J. D. Sound velocities of olivine at high pressures and temperatures and the composition of Earth's upper mantle. *Geophys Res Lett* **43**, 9611–9618 (2016).

24. Abramson, E. H., Brown, J. M., Slutsky, L. J. & Zaug, J. The elastic constants of San Carlos olivine to 17 GPa. *J Geophys Res Solid Earth* **102**, 12253–12263 (1997).
25. Mao, Z. *et al.* Elasticity of single-crystal olivine at high pressures and temperatures. *Earth Planet Sci Lett* **426**, 204–215 (2015).
26. Bouhifd, M. A., Andrault, D., Fiquet, G. & Richet, P. Thermal expansion of forsterite up to the melting point. *Geophysical Research Letters* vol. 23 1143–1146 Preprint at https://doi.org/10.1029/96GL01118 (1996).
27. Stixrude, L. & Lithgow-Bertelloni, C. Thermodynamics of mantle minerals - I. Physical properties. *Geophys J Int* **162**, 610–632 (2005).
28. Stixrude, L. & Lithgow-Bertelloni, C. Thermodynamics of mantle minerals - II. Phase equilibria. *Geophys J Int* **184**, 1180–1213 (2011).
29. Noda, M., Inoue, T., Tsuchiya, T. & Higo, Y. Reassessment of a bond correction method for in situ ultrasonic interferometry on elastic wave velocity measurement under high pressure and high temperature. *High Press Res* **42**, 278–293 (2022).
30. Darling, K. L., Gwanmesia, G. D., Kung, J., Li, B. & Liebermann, R. C. Ultrasonic measurements of the sound velocities in polycrystalline San Carlos olivine in multi-anvil, high-pressure apparatus. *Physics of the Earth and Planetary Interiors* **143**, 19–31 (2004).
31. Tange, Y., Nishihara, Y. & Tsuchiya, T. Unified analyses for P-V-T equation of state of MgO: A solution for pressure-scale problems in high P-T experiments. *J Geophys Res Solid Earth* **114**, 1–16 (2009).
32. Sinogeikin, S. V. & Bass, J. D. Single-crystal elasticity of pyrope and MgO to 20 GPa by Brillouin scattering in the diamond cell. *Physics of the Earth and Planetary Interiors* **120**, 43–62 (2000).
33. Tsujino, N. & Nishihara, Y. Effect of pressure on grain-growth kinetics of ferropericlase to lower mantle conditions. *Geophys Res Lett* **37**, n/a-n/a (2010).
34. Cook, R. K. Variation of Elastic Constants and Static Strains with Hydrostatic Pressure: A Method for Calculation from Ultrasonic Measurements. *J Acoust Soc Am* **29**, 445–449 (1957).
35. Chantel, J., Jing, Z., Xu, M., Yu, T. & Wang, Y. Pressure Dependence of the Liquidus and Solidus Temperatures in the Fe-P Binary System Determined by In Situ Ultrasonics: Implications to the Solidification of Fe-P Liquids in Planetary Cores. *J Geophys Res Planets* **123**, 1113–1124 (2018).
36. Chantel, J. *et al.* Experimental evidence supports mantle partial melting in the asthenosphere. *Sci Adv* **2**, (2016).

Figure captions

Figure 1 (double-column): (a) Schematic drawing of the ultrasonic systems used both at BGI and at P61B. Due to the acoustic impedance contrast, the elastic waves are reflected along each interface (echoes E1, E2, and E3) and propagate back to the piezoelectric crystal. The oscilloscope records that signal. Both oscilloscope and waveform generator are synchronized together to be on the same time basis (Sync. channel) and are controlled from a computer. (b) and (c) Drawings of the 14/8 (octahedral edge length to cube truncation edge length) multi-anvil assemblies used during the experiment. (b) The rhenium furnace (25 µm foil) allows to use this assembly to pressure up to 15 GPa; the B-MgO epoxy sleeve around the furnace provides good thermal insulation and is X-ray transparent. (c) The graphite heater of this assembly limits the pressure range to 8-10 GPa; here, a MgO ring is sandwiched between two ZrO_2 sleeves to manage an X-ray transparent window.

Figure 2 (single column): (a) Length of the Fresnel zone ($N = \frac{\phi_{LiNbO_3} f}{4 v_P}$, with ϕ_{LiNbO_3}, f and v_P the diameter of the transducer, the pulse frequency and the elastic wave velocity through the anvil, respectively) as a function of the transducer diameter at different fixed frequencies (see Supplementary Material S.2). The length of the Fresnel zone denotes the distance to the last acoustic pressure minimum. Vertical arrows show the resistance of transducers with 2.5 and 5 mm diameter. The anvil-BR echo should ideally be located outside of the Fresnel zone, which is matched with an ideal resistance for transducer diameters of 2.5 mm. (b) and (c) amplitude of the BR-sample reflection as a function of the sample and anvil temperature, respectively. The temperature of the transducer should be controlled to a certain extent, to limit the amplitude drop and expand the temperature of collectable data.

Figure 3 (double column): (a) and (b) Typical P- and S-wave ultrasonic echo trains. These signals correspond to data collected during BT613 at conditions of 120 bar of oil pressure load and 1173 K. These signals are represented at frequencies of 48 MHz for the P-waves and 38 MHz for the S-waves and correspond to the frequencies at which travel times were measured (see Supplementary Material S.1). (c) Typical radiography image collected during BT613 at the same conditions as (a) and (b). This image corresponds to two images stitched together, one that is centered on the sample and one that is centered on the backing plate. BR denotes the buffer rod and PM the XRD pressure markers.

Figure 4 (single column): (a) P- and (b) S-wave velocities of Fo_{90} olivine as a function of density and temperature (color code). Elastic wave velocities increase with density and decrease with temperature. (c) and (d) Comparison between the measured elastic wave velocities and the values that would be predicted from our EoS fit. Ideally, all data should align on a 1:1 line, which seems to be the case for S-waves (d) but not for the P-waves measured on BT530 (c). This is likely due to the limited frequency range that could be swept on the transducer used during the BT530 experiment, causing an apparent larger travel time, and thus a lower measured velocity. Horizontal bars correspond to two standard deviations. Red triangles show data collected using Cook's law at room temperature[30].

Figure 5 (single column): (a) Pressure evolution of the P- to S-wave velocity ratio (equivalent to the S- to P- wave travel time ratio) for Fo_{90} olivine, MgO, and Al_2O_3, and along two isotherms (300 K in full line and 1300 K in dashed line). This synthetic case was conducted using our EoS fit parameters for Fo_{90} olivine, and existing EoS literature data for MgO and Al_2O_3[28]. Shaded areas correspond to the uncertainty envelopes caused by the propagation of typical uncertainties on the P- and S-wave travel times (see Supplementary Material S.8). (b) Comparison of the pressures determined from *in-situ* X-ray diffraction data of standard materials and our novel dual travel time method, as a function of temperature. Due to small signal amplitudes at the highest temperatures and during the first steps of cooling, travel times could not be properly estimated and these data points are thus not represented. Vertical lines denote two standard deviations in pressure from the uncertainty on the travel time ratios (see Supplementary Material S.8).